THE JOURNAL OF PHYSICAL CHEMISTRY C
A JOURNAL OF THE AMERICAN CHEMICAL SOCIETY

pubs.acs.org/JPCC
Article

Interplay of Local pH and Cation Hydrolysis during Electrochemical CO_2 Reduction Visualized by In Operando Chemical Shift-Resolved Magnetic Resonance Imaging

Michael Schatz,* Johannes F. Kochs, Sven Jovanovic, Rüdiger-A. Eichel, and Josef Granwehr

Cite This: *J. Phys. Chem. C* 2023, 127, 18986−18996
Read Online

ACCESS | Metrics & More | Article Recommendations | Supporting Information

ABSTRACT: The Cu-catalyzed electrochemical CO_2 reduction enables the conversion of greenhouse gas emissions to fuels or platform chemicals with prospects of storing intermittent energy from renewable sources. While current research in tuning catalyst activity and product selectivity is often mired in finding electrode engineering solutions, the importance of electrolyte engineering is mostly overlooked. This study presents a method for measuring local pH profiles in electrode proximity and correlating them to cation-induced buffering effects. Magnetic resonance imaging (MRI) techniques were applied to evaluate the local pH values using spatially resolved ^{13}C resonances of the $CO_2/HCO_3^-/CO_3^{2-}$ equilibrium. The buffering effect of cation hydrolysis is substantiated by local shifts of the ^{23}Na resonance of Na^+ in the $NaHCO_3$ electrolytes. Steeper local pH gradients, compared to experiments with $KHCO_3$, account for increased selectivity for acetate formation from the solution-based reaction. Proven itself capable of elucidating the effect of cations on local pH values, our presented method supports tailoring the electrode−electrolyte interface to selectively generate value-added products.

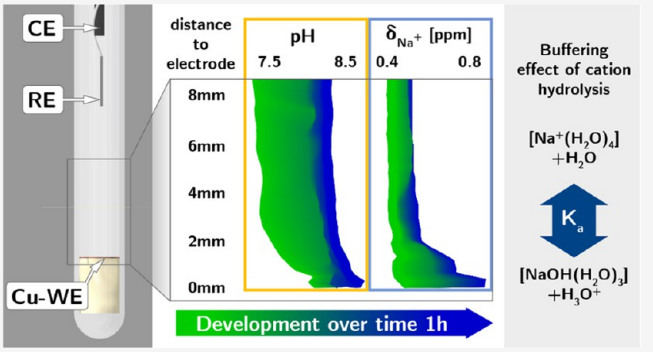

INTRODUCTION

The electrochemical CO_2 reduction (eCO_2R) by elemental copper shows the unique capability to catalyze the formation of short-chain hydrocarbons that can be utilized as fuels or base chemicals.[1,2] As the industrial application of this process may foster the storage of intermittent renewably generated power, intensive research efforts over the past decade aimed to improve catalyst materials in terms of activity and product selectivity. However, recent studies state that local reaction conditions at the electrode/electrolyte interface (EEI) play a decisive role in optimizing the catalysis of eCO_2R and, therefore, highlight the importance of engineering not only the electrode but also the electrolyte.[3−7]

The influence of local pH in electrode proximity has been demonstrated in the course of the pioneering work of Hori et al.[8] In general, increased local pH induced by consumption of H^+ at the electrode shifts selectivity toward C_{2+} products.[9] The rate-limiting step in the reaction pathway to C_{2+} products, the C−C bonding reaction, is pH-independent, which favors these pathways over the formation of products such as methane that include proton transfer in their rate-limiting step.[8,9] At the same time, the competing hydrogen evolution reaction (HER) is suppressed under proton depletion.[7,10] As a consequence of increased pH near the working electrode (WE), the solubility of the reactant CO_2 decreases.[1] Here, the importance of bicarbonate electrolytes in eCO_2R becomes evident. The conversion of CO_2 to HCO_3^- is inhibited if bicarbonate is already present in the electrolyte.[11] At the same time, bicarbonate acts as a CO_2 storage. Dunwell et al. proved that for an H-type electrolysis cell, the primary carbon source of eCO_2R was not from the direct supply of gaseous CO_2 but rather from the accelerated equilibrium between HCO_3^- and dissolved CO_2 (aq).[12]

Besides local pH effects, the impact of metal cations has been discussed recently as an integral part of the electrical double layer under negative potential.[7,13,14] Generally, improved activity and selectivity for multicarbon products of eCO_2R were observed with increasing cation size.[15−17] This was first explained by an increased potential at the outer Helmholtz plane due to enhanced specific adsorption and steric effects of larger cations.[15] However, these findings could not explain the improved eCO_2R performance to the extent observed experimentally.[7] Another mechanism was proposed by Resasco et al., who combined density functional theory (DFT) calculations with electrolysis experiments under the

Received: May 26, 2023
Revised: August 21, 2023
Published: September 15, 2023

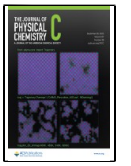

https://doi.org/10.1021/acs.jpcc.3c03563
J. Phys. Chem. C 2023, 127, 18986−18996

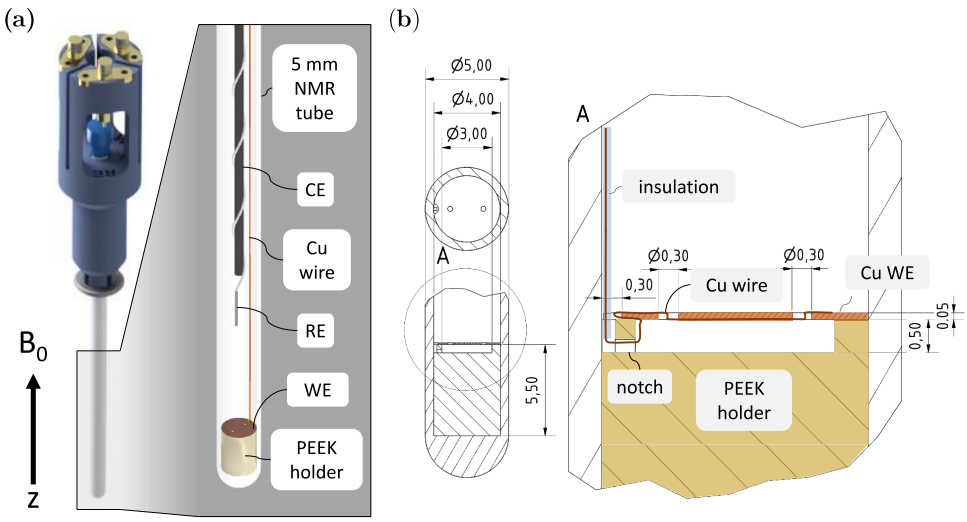

Figure 1. Electrochemical cell in a standard 5 mm NMR tube. (a) 3D model of the NMR tube in a 3D-printed sample holder with a detailed view of the inside of the cell, including WE, RE, and CE. (b) Technical drawing of the sectional top and side view of the PEEK holder for the WE with a detailed view showing the route of the contacting Cu wire.

exclusion of mass transport limitation. They discovered that crucial surface intermediates of C_{2+} products are stabilized by the electrostatic field of these hydrated cations in the outer Helmholtz plane.[17] A more recent study by Koper et al. attributed an even more substantial role to this stabilizing effect of metal cations by showing that eCO_2R was entirely suppressed in the absence of metal cations.[18] Singh et al. bridged between cation-induced effects and the impact of local pH by suggesting a buffering effect of cation hydrolysis.[16] The hydration shell of a metal cation, M^+, is dehydrated during the buffer reaction,

$$[M^+(H_2O)_n] + H_2O \rightleftharpoons [MOH(H_2O)_{n-1}] + H_3O^+ \quad (1)$$

With increasing cation size, the pK_a value of the reaction in eq 1 decreases due to increased electrostatic interaction between the cation hydration shell and the cathode and, therefore, increases the buffer capacity in the near-neutral pH region.[16] This effect was confirmed experimentally by local pH measurements using *in operando* methods, i.e., measurements performed under true catalytic conditions.[14,19] The magnitude of the buffering effect proposed by Singh et al. was found to be overestimated.[19] Increasing local pH values could be correlated to increasing cation size. The actual transformation of the hydration shell of metal cations has not been directly demonstrated. Also, there is a point of contention raised by Malkani et al., who measured decreasing local CO_2 concentrations with increasing cation size by using *in operando* infrared spectroscopy. This contradicts the assumption of enhanced buffer capacity.[20]

To gain insights into the contribution of the proposed mechanisms on the cation effects promoting eCO_2R, advanced *in operando* methods are needed to investigate the EEI more profoundly, especially in terms of the formation of valuable C_{2+} products.[6,7] However, investigating the impact of a single variable in this system is challenging, as variables interact with each other.[6] An *in operando* method is required that is capable of simultaneously measuring the local pH, local CO_2 concentration, and state of hydration of metal cations.

Spatially resolved or surface-sensitive pH measurements in electrochemical cells for eCO_2R have been approached by various *in operando* techniques.[18] Voltammetric microelectrodes[21,22] can obtain a high spatial resolution and fast response in a large pH region but have to be positioned close to the electrode and therefore influence the local reaction environment. Optical methods, such as Raman and infrared spectroscopy, are powerful noninvasive techniques for investigations of small sample volumes.[23,24] Especially, surface-enhanced Raman spectroscopy can be useful to determine the pH at the EEI based on the HCO_3^-/CO_3^{2-} equilibrium. However, this technique can be limited in spatial resolution and the detectable pH region.[18] Fluorescence microscopy can achieve an extremely high spatial resolution, enabling pH measurements in cracks within a gas diffusion electrode (GDE) for eCO_2R.[25] A fluorescent agent has to be added to the electrolyte, which is an additional variable influencing the local environment. Lu et al. presented the only study to the authors' knowledge that measured local pH gradients as a function of distance to the WE, which was a GDE in a flow cell that is optically accessible from one side.[26] Microarea Raman spectroscopy is applied to determine the HCO_3^-/CO_3^{2-} equilibrium in a 1 M KOH electrolyte, which is used to determine the local pH profile. However, the measurements showed poor quality in close electrode proximity, so the data were extrapolated to this area. Also, the amount of dissolved CO_2 (aq) could not be determined and was, therefore, calculated using theoretical considerations.

In this work, a method is presented that addresses these challenges by employing *in operando* nuclear magnetic resonance (NMR) and magnetic resonance imaging (MRI) techniques. Hereby, the ^{13}C and ^{23}Na resonances of the bicarbonate electrolyte are assessed in terms of the local chemical environment at a Cu WE. Our previously described pH determination method[27] is extended by the application of MRI pulse sequences while maintaining spectroscopic information. The ^{13}C measurements are thereby spatially resolved, enabling the observation of the evolution of the concentration profiles of the HCO_3^-/CO_3^{2-} equilibrium as well as of dissolved CO_2 (aq), which are then utilized to determine the local pH profiles. ^{23}Na images are acquired alternatingly with ^{13}C when using $NaHCO_3$ electrolytes to study changes in the chemical environment of Na^+ cations. By comparing $NaHCO_3$ with $KHCO_3$ electrolytes of varying

https://doi.org/10.1021/acs.jpcc.3c03563
J. Phys. Chem. C 2023, 127, 18986−18996

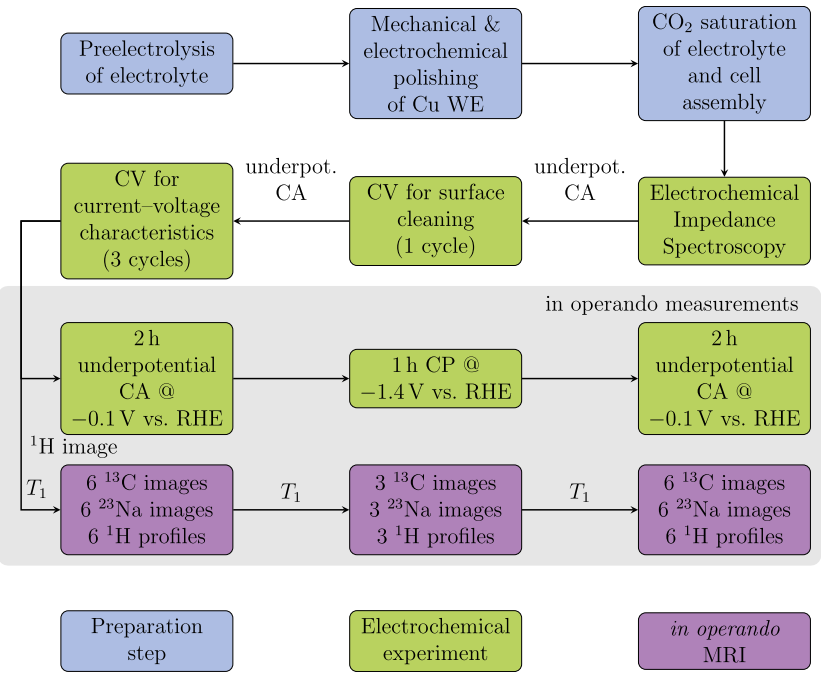

Figure 2. Experimental protocol including all preparation steps, the electrochemical experiments conducted before and during *in operando* measurements, and all NMR and MRI experiments. Electrical impedance spectroscopy measurements were utilized to inspect electrical connections within the setup. ^{1}H images were acquired at the start of *in operando* measurements. "T_1" marks T_1 measurements of the ^{13}C resonances in the experimental protocol, which were used to correct the ^{13}C signal intensities.

concentrations, the influences of buffer capacity and cation size are discriminated.

EXPERIMENTAL METHODS

The experimental *in operando* NMR setup including shielding, grounding, and filters were adopted from our previous publications.[27,28] The electrochemical cell in a 5 mm NMR tube was adjusted to meet the requirements for MRI. The Bruker DiffBB broadband gradient probe, operated on a Bruker Avance III HD spectrometer (Bruker BioSpin GmbH, Rheinstetten, Germany) with a 14.1 T wide-bore magnet, offers magnetic field gradients along the longitudinal axis of the NMR tube. Placing the Cu WE perpendicularly to the direction of these gradients, as depicted in Figure 1a, profiling as a function of distance from the WE is simplified to a single dimension due to rotational symmetry about the *z*-axis. The position of the WE is fixed by a holder made of chemically inert poly(ether ether ketone) (PEEK). To inhibit contact of the aerophilic PEEK surface with the electrolyte that would otherwise favor bubble adhesion in the sensitive NMR volume, the WE is punched out from Cu foil (Goodfellow GmbH, Hamburg, Germany) to 4 mm in diameter and placed on top of the holder, as illustrated in Figure 1a. To remove the constriction of the inner diameter at the top of NMR tubes and fit their 4 mm inner diameter exactly, standard NMR tubes were shortened to ca. 130 mm total length. The stripped end of an insulated Cu wire (Goodfellow GmbH, Hamburg, Germany) secures the WE on the holder and simultaneously contacts it electrically, cf. the technical drawing in Figure 1b. Moreover, the adjusted position of the WE is parallel to the exciting radiofrequency (RF) field, which minimizes distortions due to eddy currents induced in the conductive WE.[28−30] 1 M stock solutions of ^{13}C-enriched $NaHCO_3$ and $KHCO_3$ (98 atom %, Sigma-Aldrich Chemie GmbH, Munich, Germany) were treated by preelectrolysis using two Pt mesh electrodes as WE and CE at 0.025 mA/cm^2 over 16 h under a N_2 atmosphere.[31] The Cu WE was mechanically and electrochemically polished.[32] These treatments conformed with relevant studies in this field.[2,33] The WE was inserted into the NMR tube, and then 500 μL of the electrolyte, diluted to the desired concentrations of 1, 0.5, and 0.1 M, was filled in. The solution was then bubble-saturated at 10 °C with ^{13}C-enriched CO_2 (≥97 atom %, CortecNet, Les Ulis, France). A glassy carbon rod (HTW GmbH, Thierhaupten, Germany) was introduced as a counter electrode (CE) and a chlorinated silver wire served as a reference electrode (RE). CE and RE were placed in the tube above the NMR-sensitive volume in order to minimize distortions of the RF pulse. The tube was closed with a PE cap and sealed with Parafilm. The contacting wires were connected to the respective electrode of the potentiostat via SMA connectors at the top of a dedicated sample tube holder. Finally, the cell was introduced into the NMR probe that was prechilled at 10 °C. The tube was placed such that the WE was located 5 mm below the center of the sensitive volume of the detection coil in the probe.

The protocol used for electrochemical experiments before and during the *in operando* measurements is illustrated in Figure 2. Preliminary electrochemical measurements include impedance spectroscopy, cyclovoltammetry (CV) for surface cleaning of the WE, and three additional CV cycles to determine the current−voltage characteristics. From the last CV cycle, the current strength that is applied during chronopotentiometry (CP) is selected to result in electrolysis condition at ca. − 2.2 V versus Ag/AgCl, i.e., ca. − 1.4 V versus RHE. Consequently, a current density of $-1.37 \pm 0.29 \frac{\mathrm{mA}}{\mathrm{cm}^2}$ was applied for 0.1 M initial electrolyte concentration, as well as $-5.7 \pm 2.3 \frac{\mathrm{mA}}{\mathrm{cm}^2}$ for 0.5 M and $-7.8 \pm 1.6 \frac{\mathrm{mA}}{\mathrm{cm}^2}$ for 1 M. In

https://doi.org/10.1021/acs.jpcc.3c03563
J. Phys. Chem. C 2023, 127, 18986−18996

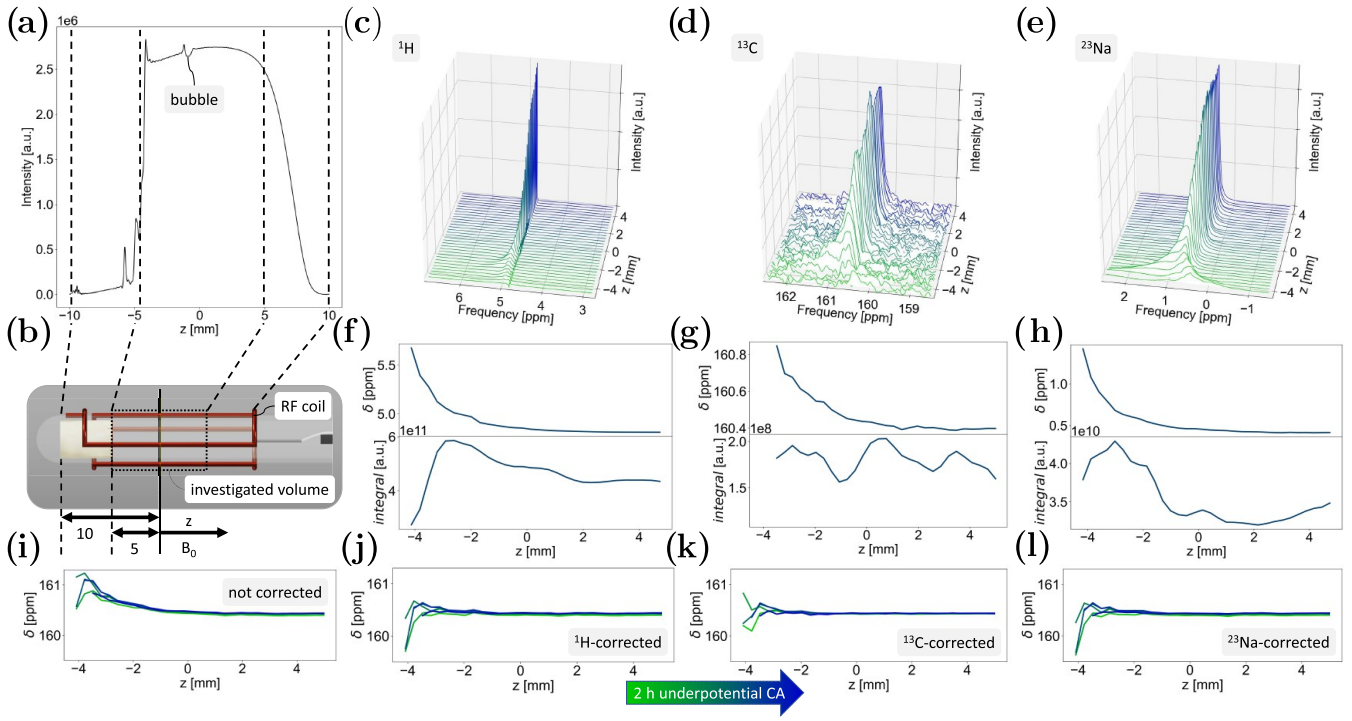

Figure 3. Chemical shift imaging (CSI) profiles of a 1 M $NaHCO_3$ electrolyte in the *in operando* cell illustrate a nucleus-independent chemical shift due to magnetic field distortions. (a) Frequency-encoded ^1H image shows the intensity profile along the *z*-axis in the sensitive volume depicted in schematic (b). The location of the electrode is shown relative to the sensitive volume and the *z*-axis. The volume with uniform excitation above the WE investigated in the following measurements corresponds to a length of ca. 10 mm on the *z*-axis. (c–e) Spatially resolved CSI spectra of the ^1H resonance of water (c), the ^{13}C resonance of carbonate (d), and the ^{23}Na resonance of Na^+ (e). ^{13}C spectra were processed with 10 Hz line broadening for better visualization in terms of signal-to-noise ratio. (f–h) Chemical shift and integral as a function of *z* of peaks fitted to the spectra depicted in (c–e), respectively. (i–k) Evolution of the carbonate chemical shift (CCS) during underpotential CA before electrolysis without correction (i) and corrected using the chemical shift profiles in (f–h), respectively.

between every measurement, underpotential chronoamperometry (CA) at −0.9 V versus Ag/AgCl, corresponding to ca. −0.1 V versus RHE, is applied to keep the WE at negative potential and, therefore, inhibit reoxidation of the Cu surface.[34]

Before tuning and shimming, ^1H profiles were recorded using a frequency-encoded pulse sequence optimized for imaging of electrochemical cells[35] to check whether the sensitive volume was bubble-free. Details are provided in Section S1 in the Supporting Information (SI). To maintain spectroscopic information about the ^{13}C and ^{23}Na resonances, a pure phase-encoded chemical shift imaging (CSI) pulse sequence using spin echoes and single-point imaging was employed. Magnetic susceptibility artifacts could be reduced by applying phase-encoded rather than frequency-encoded imaging techniques as well as by employing increased gradient strengths for spatial encoding. Despite its increased experiment time, single-point imaging is advised for short T_2 relaxation times.[36] By using spin echoes, phase errors due to magnetic field inhomogeneities are refocused. Also, the transversal magnetization relaxes with the time constant $T_2 \geq T_2^*$. However, due to the low sensitivity of ^{13}C measurements, echo times were kept as short as hardware limitations permitted, resulting in minimum echo time and therefore short gradient pulses. This in turn had the advantageous effect of maximizing the gradient strength, which minimized magnetic field artifacts. Details about the pulse sequence and acquisition parameters are given in Section S1 in the SI. The full code of the pulse sequence for Bruker Topspin is available in Section S7 in the SI.

Long T_1 relaxation times of the ^{13}C resonance of CO_2 on the order of 10–20 s led to a trade-off between experiment time and CO_2 sensitivity. As CO_2 was consumed during the reaction, the signal intensity decreased below the detection limit. Complete relaxation would have required a repetition time of 50–100 s, resulting in a total experiment duration for the ^{13}C image on the order of hours. As such experiment duration would rule out observations of dynamic changes in the electrolyte, the repetition time was set to 9 s; hence, the experiment time with 32 *k*-space points and a four-step phase cycle was 19 min. Though during this time, mixing due to diffusion and magnetohydrodynamic convection was expected, the acquisition time mainly consisting of the decay time of the NMR signal was on the order of one second. Hence, when experiments are carried out in a quasi-steady state, the point spread function is influenced by mobility on time scales of 1 s rather than 19 min. To correct the intensity errors of the CO_2 and coalesced HCO_3^-/CO_3^{2-} resonances, T_1 was measured before each step of the *in operando* measurements, cf. Figure 2, and corrected accordingly for the pH evaluation, cf. Section S3 in the SI. ^{23}Na nuclei typically relax significantly faster. Repetition times of less than 0.2 s were sufficient, and a ^{23}Na image was acquired within 48 s. Therefore, the combined experiment duration of ^{13}C and ^{23}Na images was approximately 20 min, with some minor variability caused by varying durations of the automatic tuning and matching that was typically conducted within ca. 10–30 s.

After all NMR parameters were set up and a bubble-free sensitive volume was ensured, a ^1H CSI image was acquired as

https://doi.org/10.1021/acs.jpcc.3c03563
J. Phys. Chem. C 2023, 127, 18986–18996

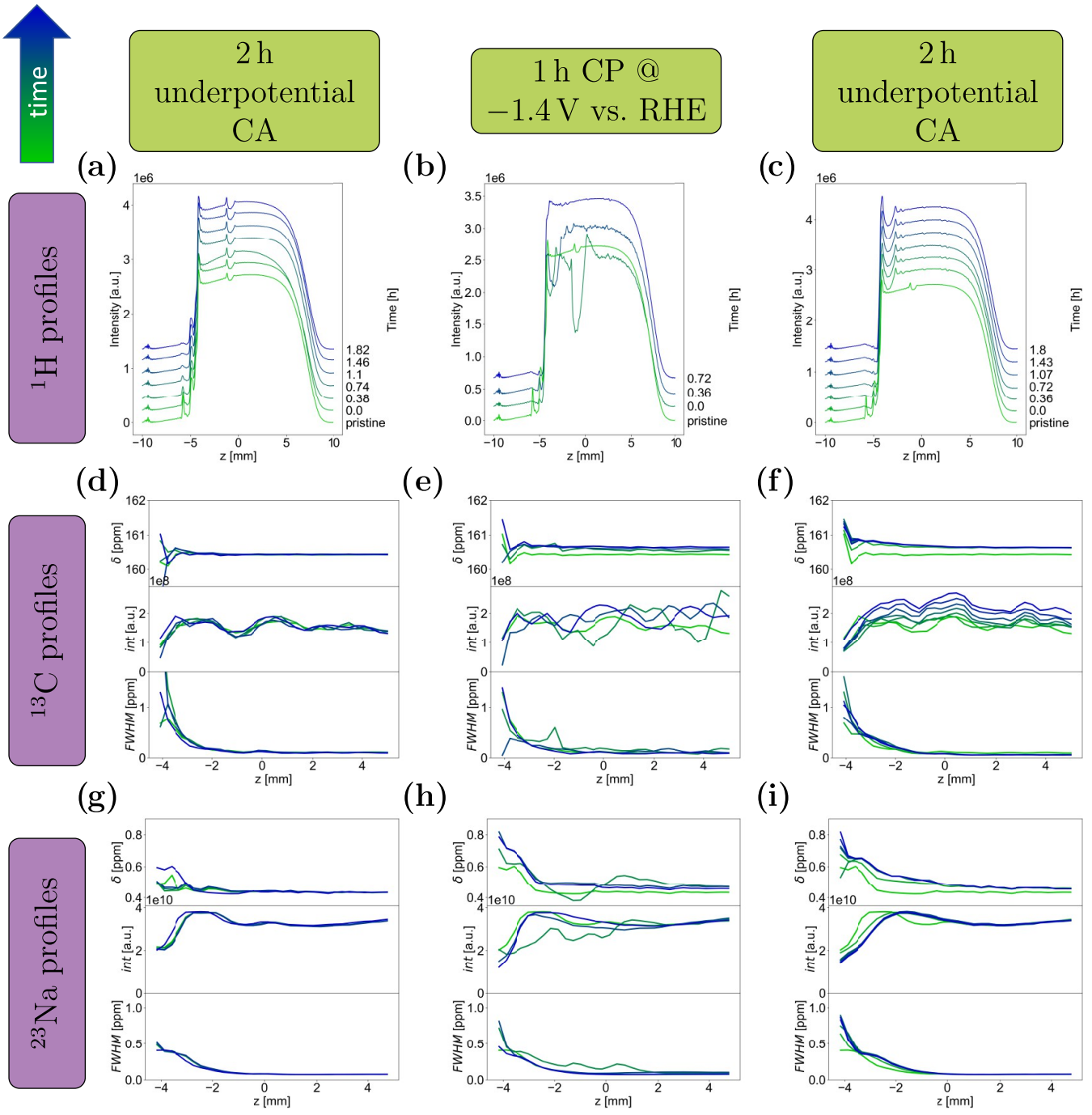

Figure 4. Exemplary *in operando* experiment with 1 M $NaHCO_3$. (a–c) Evolution of frequency-encoded ^{1}H profiles before (a), during (b), and after (c) electrolysis. (d–f) Evolution of phase-encoded ^{13}C CSI images before (d), during (e), and after (f) electrolysis. (g–i) Evolution of phase-encoded ^{23}Na CSI images before (g), during (h), and after (i) electrolysis. Evolution of profiles over time is represented from green to blue color. For reference, the last profiles acquired before electrolysis (a), (d), and (g) were repeated as first profiles in bright green in the plots representing the measurements during electrolysis (b), (e), (h) and after electrolysis (c), (f), (i).

a reference. The *in operando* measurements started with 2 h of underpotential CA at −0.1 V versus RHE, during which six ^{13}C images were acquired. In the case of the $NaHCO_3$ electrolyte, six additional ^{23}Na images were recorded alternately. Between these measurements of varying nuclei using the same broadband channel of the probe, the resonator circuit was automatically tuned and matched to the Larmor frequency of the respective nucleus. Additionally, before every ^{13}C image, a frequency-encoded ^{1}H profile was acquired to estimate the influence of bubbles on the CSI measurements.

The raw data were processed as described in Section S2 in the SI. The spatially resolved ^{1}H resonances of water, ^{13}C resonances of CO_2 and coalesced HCO_3^-/CO_3^{2-}, and ^{23}Na resonances of Na^+ were fitted using Lorentzian functions, providing their respective chemical shift, integral, and full width at half-maximum (fwhm) for further evaluation.

As previously described,[27] the pH evaluation was performed based on the acquired chemical shift of the coalesced HCO_3^-/CO_3^{2-} resonance, which will be denoted as the carbonate chemical shift (CCS), as well as the fitted integrals of the CO_2

https://doi.org/10.1021/acs.jpcc.3c03563
J. Phys. Chem. C 2023, 127, 18986−18996

and HCO_3^-/CO_3^{2-} resonances. Below the threshold value of pH = 7.4, the following Henderson–Hasselbalch equation was used

$$\mathrm{pH} = \mathrm{p}K_{a2} + \log_{10}\frac{[HCO_3^-]}{[CO_2]} \quad (2)$$

The pK_{a2} value for the equilibrium reaction between CO_2 and HCO_3^- was determined as pK_{a2} = 6.467 for a temperature of 10 °C using literature data.[37] Above the threshold pH, a variation of the Henderson–Hasselbalch equation describing the equilibrium reaction between HCO_3^- and CO_3^{2-} based on the CCS was applied

$$\mathrm{pH} = \mathrm{p}K_{a1} + \log_{10}\left|\frac{\delta_c - \delta_{HCO_3^-}}{\delta_c - \delta_{CO_3^{2-}}}\right| \quad (3)$$

Here, pK_{a1} was determined as 9.645 and the chemical shifts of pure HCO_3^- and CO_3^{2-} were $\delta_{HCO_3^-}$ = 163.27 ppm and $\delta_{CO_3^{2-}}$ = 171.01 ppm, respectively, where acetonitrile in a separated capillary was used as an NMR reference to define the chemical shift axis. As no NMR reference was used in the adjusted cell setup to ensure the maximum sensitivity of measurements, the function describing the correlation of CCS and the pH value had to be calibrated to match the initial CCS with the initial pH value in the sample. The pH value in the electrolyte after CO_2 saturation was determined using a benchtop Mettler–Toledo FiveEasy F20 pH meter with a standard probe (Mettler–Toledo GmbH, Giessen, Germany). The measured pH averaged 6.71 ± 0.04 for 0.1 M, 7.25 ± 0.07 for 0.5 M, and 7.58 ± 0.03 for 1 M $NaHCO_3$ and $KHCO_3$ solutions.

After the *in operando* measurements were conducted, electrodes were removed and the deuterated NMR reference trimethylsilylpropanoic acid (TSP) was added to the NMR tube to result in a concentration of 1 mM. The product analysis was performed using ^{1}H NMR with water suppression.[27,38]

RESULTS AND DISCUSSION

Correction of Chemical Shift Profiles. Figure 3a represents an exemplary frequency-encoded ^{1}H profile of the electrochemical cell. The placement of the cell relative to the NMR-sensitive volume is shown in Figure 3b, where the origin of the *z*-axis is set at the center of the sensitive volume. The electrode was placed accordingly at $z = -5$ mm. Thus, the sharp increase in intensity above $z = -5$ mm corresponds to the high proton density of the aqueous electrolyte. The decrease in intensity at $z \geq 5$ mm is due to the sensitivity loss of the probe toward the boundaries of the sensitive volume. Therefore, the volume investigated in the following discussion is restricted to about 10 mm above the WE along the *z*-axis, where the excitation is approximately homogeneous. This intrinsic RF field inhomogeneity of the sensitive volume is due to the BBO version of the DiffBB probe used in this study. Here, the ^{1}H coil encloses the broadband coil; hence, it is not optimized for ^{1}H but instead for broadband nucleus field homogeneity.

The resulting images of CSI measurements of the ^{1}H resonance of water, the ^{13}C carbonate resonance, and the ^{23}Na resonance of Na^+ in a 1 M $NaHCO_3$ electrolyte are depicted in Figure 3c–e, respectively. The corresponding chemical shift and integral profiles along the *z*-axis are depicted in Figure 3f–h, respectively. In all experiments, an initially increased CCS was observed in electrode proximity on the order of about 0.5 ppm. This effect was also observed in the ^{23}Na images and in the ^{1}H images recorded as a reference before the *in operando* measurements, cf. Figure 3c–e, respectively. Therefore, this nucleus-independent chemical shift was assigned to variations of the static magnetic field as a result of inhomogeneities induced by the conductive WE and the contacting Cu wire as well as imperfect magnetic field homogenization by shimming. As the CCS is crucial for pH determination, a correction was required, which assumes a uniform spatial distribution of the pH value and therefore also of the CCS along the *z*-axis measured in the CO_2-saturated electrolyte. The uncorrected CCS profiles in Figure 3i during underpotential CA before electrolysis are compared to corrected CCS profiles using the ^{1}H chemical shift profile of water, the initial ^{13}C CCS profile, and the ^{23}Na chemical shift profile of Na^+, depicted in Figure 3j–l, respectively. The CCS was evenly distributed in all corrected profiles at the start of measurements, as expected if no external electric field was applied. An increase in CCS near the electrode evolved over 2 h of underpotential CA before electrolysis. All following ^{13}C CCS profiles were, therefore, corrected with the initially acquired ^{13}C image, and all ^{23}Na profiles accordingly with the initially acquired ^{23}Na image.

^{13}C and ^{23}Na Images under Underpotential and Electrolytic Conditions. The evolution over time of the frequency-encoded ^{1}H profiles, as well as ^{13}C and ^{23}Na images at −1.4 V versus RHE, is depicted for the 1 M $NaHCO_3$ electrolyte in Figure 4. An estimation of errors and uncertainties is given in Section S4 in the SI. During the underpotential CA before electrolysis, no significant changes in the ^{1}H profiles were observed. An initially decreased intensity in the profile at ca. z = 3 mm was attributed to a single bubble attached to the insulated Cu wire. The profile peaks at the position of the electrode, which is assumed to be an effect of magnetic field distortions in the proximity of conductive components. Both the ^{13}C and ^{23}Na images develop toward an equilibrium state. During 1 h under electrolysis conditions, ^{1}H profiles indicate large bubbles formed in the sensitive volume. These findings can be interpreted as snapshots of the cell as the acquisition time is short with ca. 10 s. Similarly, severe disruptions of the ^{13}C profiles were not observed as errors induced by bubbles in the sensitive volume averaged out over the relatively long acquisition time. Still, uncertainties in the course of the profiles could not be entirely precluded. ^{23}Na images were rather prone to distortions as a result of bubble formation and adhesion due to their shorter acquisition time. The quality of the data had to be assessed individually by comparing the ^{23}Na profiles with the ^{1}H profiles.

Carbonate and Na^+ showed a general trend of increasing chemical shifts along the whole *z*-axis during electrolysis, with an increased gradient toward the electrode. The maximum changes after 1 h electrolysis in ^{13}C and ^{23}Na shift were on the order of 0.5 and 0.2 ppm, respectively. This rules out a magnetic field-induced change of chemical shift, which would otherwise result in quantitatively equal changes in the chemical shift of various nuclei. The increase in CCS could thus be attributed to an increase in local pH. Notably, the largest change in CCS occurred at the start of the electrolysis. Toward the end, chemical shift profiles evolved toward an upper limit, which suggests the mixing of the volume in electrode proximity with the bulk electrolyte. This finding indicates that a convective flow is induced in the cell due to magneto-hydrodynamic forces[39] or local heating. Such a flow would also

https://doi.org/10.1021/acs.jpcc.3c03563
J. Phys. Chem. C 2023, 127, 18986–18996

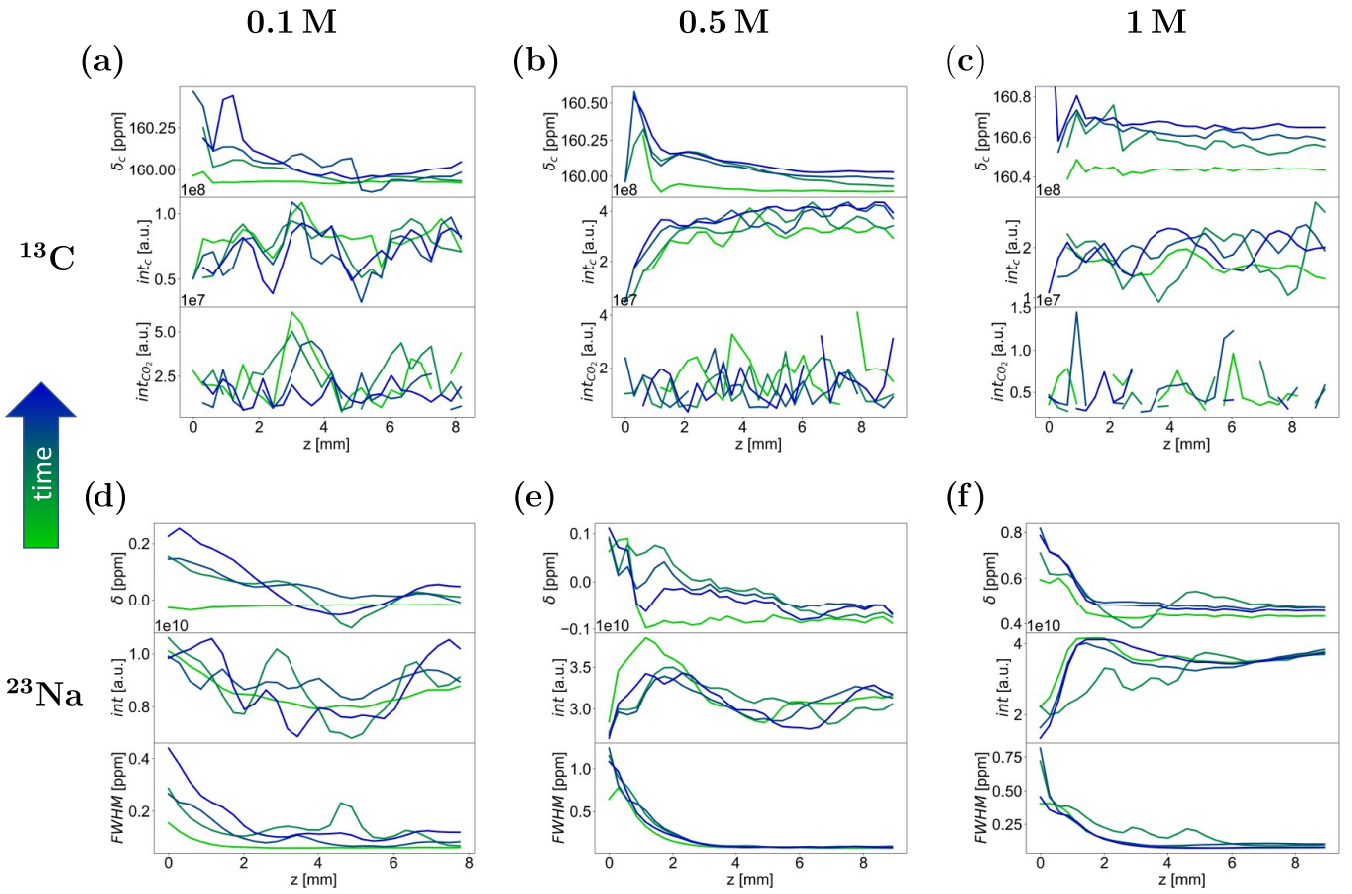

Figure 5. Results of ^{13}C and ^{23}Na CSI measurements during electrolysis at ca. −1.4 V versus RHE with 0.1, 0.5, and 1 M $NaHCO_3$ electrolytes. (a−c) Chemical shift and integral of ^{13}C carbonate resonance and integral of ^{13}C CO_2 resonance as a function of distance to the electrode for 0.1 M (a), 0.5 M (b), and 1 M (c) initial $NaHCO_3$ concentrations. (d−f) Chemical shift integral and fwhm of ^{23}Na resonance of Na^+ as a function of distance to the electrode for 0.1 M (d), 0.5 M (e), and 1 M (f) initial $NaHCO_3$ concentration. The origin of the *z*-axis is set at the position of the WE. The evolution of profiles over time is represented from green to blue color.

enhance the detachment of bubbles in the sensitive volume.[40] Concentration changes at the beginning of electrolysis were reflected by the potential decrease during CP depicted in Figure S7a. After about 20 min, a steady-state equilibrium is reached. This equilibration is also evident in the CCS profiles, which exhibited a notable increase during the acquisition of the initial image spanning the first 19 min of electrolysis. Subsequently, these profiles demonstrated minimal alterations as the experiment progressed. Consequently, although the time resolution implies some averaging artifacts during the initial minutes, it is adequate for the majority of the experiment. Lastly, it is noted that the CO_2 signal intensity decreased below the detection limit in WE proximity during electrolysis.

After electrolysis, the cell was operated under underpotential CA, where, in accordance with the previous CA phase, only minor changes in the profiles were observed. However, there is a persistent difference between the profiles before electrolysis, indicated by a bright green color, and after electrolysis, indicated by a dark green to blue color, depicting an overall increased pH of the cell. Increasing integrals of the carbonate resonances may also be affected by a decrease of T_1 relaxation times that occurs during electrolysis and is therefore not considered in the correction.

Figure 5 compares the fitted parameters of ^{13}C and ^{23}Na images of experiments with 0.1, 0.5, and 1 M $NaHCO_3$ electrolytes during electrolysis. For the discussion of errors in CSI measurements, systematic and statistical errors were distinguished. Systematic errors resulting from peak broadening and peak fitting are presented in Figures S2−S5 in Section S4 in the SI, supplementing Figure 5. Standard deviations from statistical averaging of three repeated experiments are given in the results of pH profile determination, Figure 6, and product analysis, Section S6.

In the exemplary experiments presented in Figure 5, an increase of the chemical shifts and integrals of carbonate, as well as a simultaneous decrease in the CO_2 integral, implies increased local pH in all cases, but to a varying extent. The ^{23}Na images show increased chemical shifts, while integral and width remain unaltered except for outliers due to bubbles in the sensitive volume. The ^{23}Na shift of Na^+ cations was found to be concentration-dependent.[41] However, the integral profiles in the presented experiments remained essentially constant during electrolysis and could therefore not account for this effect. In contrast, the buffering effect of cation hydrolysis proposed by Singh et al.,[16] cf. eq 1, offers an explanation for these observations. A fully hydrated Na^+ cation is accompanied by four H_2O molecules in its hydration shell. DFT calculations showed that the deprotonation of $Na^+(H_2O)_n$ clusters, where n represents the hydration number, leads to a downfield shift of the ^{23}Na resonance of Na^+.[42] In particular, the chemical shift difference between n = 4 and n = 3 was calculated to be 7.1 ppm. Here, we observe a downfield

https://doi.org/10.1021/acs.jpcc.3c03563
J. Phys. Chem. C 2023, 127, 18986−18996

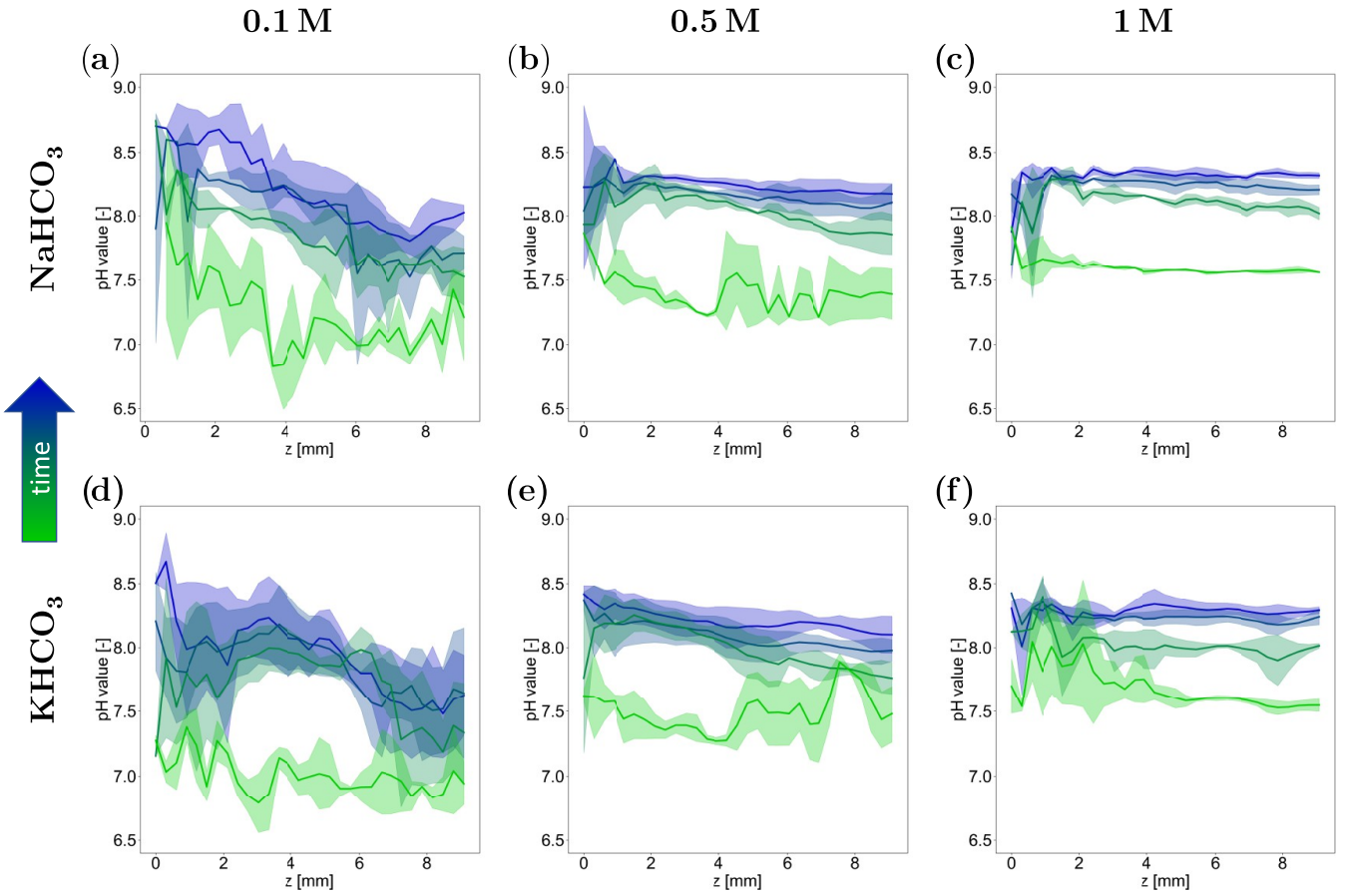

Figure 6. Mean pH profiles and standard errors from three repeated experiments during electrolysis at ca. −1.4 V versus RHE with 0.1 M (a), 0.5 M (b), and 1 M (c) $NaHCO_3$ electrolytes, and 0.1 M (d), 0.5 M (e), and 1 M (f) $KHCO_3$ electrolytes. The origin of the *z*-axis is set at the position of the WE. The evolution of profiles as a function of time is represented from green to blue color.

shift on the order of 0.1−0.2 ppm. According to eq 1, this could be explained by a small amount of $Na^+(H_2O)_3$ formed by deprotonation in fast chemical equilibrium with $Na^+(H_2O)_4$. Therefore, only one coalesced resonance is observed, that is, the weighted average of the Na^+ signals with hydration numbers $n = 3$ and $n = 4$, which range between 0 and 7.1 ppm.

Figure 6 depicts the evolution of pH profiles during electrolysis at −1.4 V versus RHE, determined from the chemical shifts and integrals of carbonate, as well as CO_2 integrals. This figure contrasts experiments with $NaHCO_3$ and $KHCO_3$ electrolytes at concentrations of 0.1, 0.5, and 1 M. In all experiments, a significant increase in local pH was detected. The largest pH changes were observed for the least buffered 0.1 M electrolytes, ranging from roughly 6.6 to 8.5. The 1 M electrolytes spanned a pH range from 7.6 to 8.5. Error bars in Figure 6 were relatively small, especially for 0.5 and 1 M initial concentrations, confirming the statistical significance of the presented experiments. For all three concentrations, the local pH values measured for the $NaHCO_3$ electrolyte were higher than those for $KHCO_3$. Also, the experiments with Na^+ cations evolved a pH gradient higher than those with K^+. The additional buffering capacity due to the decreased pK_a of the cation hydrolysis of K^+ compared to that of the smaller Na^+ cations may also account for this effect. Singh et al. reported a cathode pH of 8.5 for 0.1 M $NaHCO_3$, which is in accordance with the present study, while the pH reported for 0.1 M $KHCO_3$ was 7.3, which is lower than our measured pH of approximately 8. Our study agrees with the findings of Ayemoba et al.,[19] who measured local pH values of ca. 8.7 for $NaHCO_3$ and ca. 8 for $KHCO_3$, confirming the overestimation of the buffering effect of K^+ by Singh et al.

Product Analysis. The effect of cation variation on product selectivity is manifested in the ex situ analysis of liquid products formed during *in operando* experiments. Figure 7a,b shows the product analysis in terms of concentration and Faradaic efficiency (FE), respectively, given as mean values from three repeated experiments. For reasons of clarity and comprehensibility, statistical errors are presented in Tables S3 and S4 in the SI. For the calculations of the FE of the formed liquid products, residuals of impurities in the pristine solutions were subtracted from the product concentrations.[27] In general, formate, acetate, dissolved methane, and acetaldehyde were detected in all samples. The most pronounced difference between product distributions with $NaHCO_3$ and $KHCO_3$ electrolytes was that alcohols, i.e., ethanol and, to a lower extent, methanol, were found only in $KHCO_3$ electrolytes, while the FE for acetate was larger for $NaHCO_3$ electrolytes. Increased FE for ethanol and formate for larger metal cations in bicarbonate electrolytes was also confirmed in earlier studies.[15−17] The highest FE for formate was observed for the least buffered 0.1 M solutions, which is in accordance with literature data.[1] However, increased acetate formation was not observed for Na^+ or smaller cations. Instead, it was only detected for larger cations.[16] Recently, Heenen et al. presented a mechanism for acetate formation via a solution-based

https://doi.org/10.1021/acs.jpcc.3c03563
J. Phys. Chem. C 2023, 127, 18986−18996

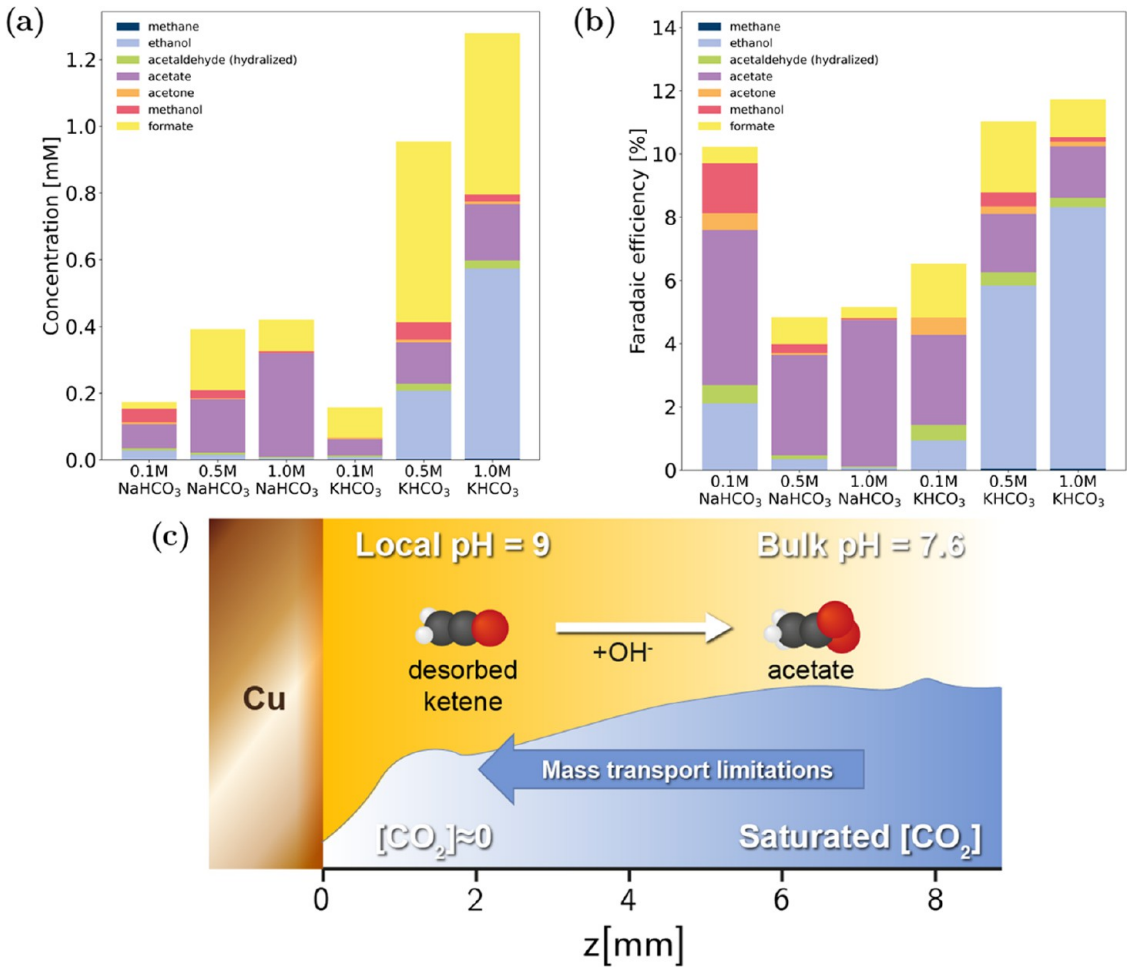

Figure 7. Product analysis using ex situ ^{1}H NMR with water suppression. (a) Concentrations of products detected in liquid solutions of 0.1, 0.5, and 1 M $NaHCO_3$ and $KHCO_3$ after *in operando* experiments at ca. −1.4 V versus RHE and concentrations of impurities detected in pristine $NaHCO_3$ and $KHCO_3$ electrolytes. (b) Resulting Faradaic efficiencies of eCO_2R products for 0.1, 0.5, and 1 M $NaHCO_3$ and $KHCO_3$ electrolytes. Values are given as the average of three repeated experiments. Statistical errors are presented in Tables S3 and S4 in the SI. (c) Schematic of the solution-based acetate formation mechanism proposed by Heenen et al.,[43] applied to the presented *in operando* experiments.

reaction of ketene with OH^-,[43] that is schematically depicted in Figure 7c. As it evolves as a homogeneous reaction in the electrolyte, it is favored under highly basic conditions and is governed by transport effects. They also stated that more positive potentials, i.e., ≥ −1.2 V versus SHE, as well as more negative potentials, i.e., < −1.5 V versus SHE, supported this reaction, which applies to the described experiments at ca. −1.78 V versus SHE. Since no external mixing was applied except for magnetohydrodynamic convection and since CO_2 signals decreased below the detection limit, it is assumed that the transport of reactants was limited. Ketene intermediates could therefore desorb into the solution and could further react to acetate. The increased local pH gradients found in the presented measurements in $NaHCO_3$ electrolytes compared to $KHCO_3$ were due to the interplay of OH^- production, proton consumption, and solution phase reactions with OH^- caused by the limited mass transport conditions.[6] Thus, steep pH gradients can be an indicator for an enhanced solution-based reaction to acetate. Interestingly, a similar contradiction to expectations of local CO_2 concentration was noticed by Malkani et al.[20] With an increased buffer capacity of larger cations, a higher interfacial CO_2 concentration is expected. However, the CO_2 resonances stay longer above the detection limit for the less buffered $NaHCO_3$ electrolytes. As the total FE of eCO_2R for $KHCO_3$ electrolytes is higher than that for $NaHCO_3$ despite lower CO_2 availability, it is suggested that larger cations accelerate eCO_2R regardless of decreased interfacial CO_2 solubility.[20]

CONCLUSIONS

This study introduces a new method for spatially resolved local pH determination in a bicarbonate electrolyte based on the ^{13}C resonances of the $CO_2/HCO_3^-/CO_3^{2-}$ equilibrium. By variation of the electrolyte concentration and cation identity, the various buffer capacities of the electrolytes could be visualized under CO_2 reductive conditions at a Cu electrode. Using ^{23}Na profiles, a decreased local pH could be attributed to an increased buffering effect of cation deprotonation for larger cations. As predicted by theoretical calculations, we provided experimental evidence of the deprotonation of the cation hydration shell during electrolysis. Furthermore, an increased FE for acetate was stated for $NaHCO_3$ electrolytes and could be correlated with steep pH gradients by considering the mechanism of a solution-based reaction of ketene intermediates with OH^-. However, the results confirmed that the buffering effect of the cation hydrolysis alone cannot be accountable for the increased activity and selectivity of eCO_2R

https://doi.org/10.1021/acs.jpcc.3c03563
J. Phys. Chem. C 2023, 127, 18986−18996

with increasing cation size. The differences in local pH profiles when comparing $KHCO_3$ and $NaHCO_3$ electrolytes were not substantial enough to account for the variations in product distributions. As recently reported, stabilization of eCO_2R intermediates and interfacial electric field effects remain the most important explanations of cation effects.[18] Nonetheless, the presented method has the potential to help engineer not only the electrode but also the electrolyte and, therefore, tailor the EEI. For example, by mixing electrolytes or by using nonaqueous electrolytes, the desired product distribution and selectivity may be tuned by determining local reaction conditions.[3] To effectively contribute to the engineering of EEIs, the greatest challenge is to overcome the mass transport limitations intrinsic to the presented operando cell design.

■ ASSOCIATED CONTENT

Supporting Information

The Supporting Information is available free of charge at https://pubs.acs.org/doi/10.1021/acs.jpcc.3c03563.

Details on pulse sequences; data processing and correction; error estimation; and electrochemical performance of the cell (PDF)

■ AUTHOR INFORMATION

Corresponding Author

Michael Schatz − *Institute of Energy and Climate Research, Fundamental Electrochemistry (IEK-9), Forschungszentrum Jülich, 52428 Jülich, Germany; Institute of Technical and Macromolecular Chemistry, RWTH Aachen University, 52056 Aachen, Germany;* orcid.org/0000-0002-5287-8769; Email: m.schatz@fz-juelich.de

Authors

Johannes F. Kochs − *Institute of Energy and Climate Research, Fundamental Electrochemistry (IEK-9), Forschungszentrum Jülich, 52428 Jülich, Germany*

Sven Jovanovic − *Institute of Energy and Climate Research, Fundamental Electrochemistry (IEK-9), Forschungszentrum Jülich, 52428 Jülich, Germany;* orcid.org/0000-0002-1227-4936

Rüdiger-A. Eichel − *Institute of Energy and Climate Research, Fundamental Electrochemistry (IEK-9), Forschungszentrum Jülich, 52428 Jülich, Germany; Institute of Physical Chemistry, RWTH Aachen University, 52056 Aachen, Germany;* orcid.org/0000-0002-0013-6325

Josef Granwehr − *Institute of Energy and Climate Research, Fundamental Electrochemistry (IEK-9), Forschungszentrum Jülich, 52428 Jülich, Germany; Institute of Technical and Macromolecular Chemistry, RWTH Aachen University, 52056 Aachen, Germany*

Complete contact information is available at: https://pubs.acs.org/10.1021/acs.jpcc.3c03563

Notes

The authors declare no competing financial interest.

■ ACKNOWLEDGMENTS

The authors thank Philipp M. Schleker for technical assistance and fruitful discussion and Sebastian B.C. Lehmann for graphical support, in particular for Figure 7c and the TOC. This research has been supported by the German Research Foundation (DFG) under Germany's Excellence Strategy—Cluster of Excellence 2186 "The Fuel Science Center" (grant no. 390919832).

■ REFERENCES

(1) Hori, Y. *Modern Aspects of Electrochemistry*; Vayenas, C. G.; White, R. E.; Gamboa-Aldeco, M. E., Eds.; Springer-Verlag: s.l., 2008; Vol. *42*, pp 89−189.

(2) Kuhl, K. P.; Cave, E. R.; Abram, D. N.; Jaramillo, T. F. New insights into the electrochemical reduction of carbon dioxide on metallic copper surfaces. *Energy Environ. Sci.* **2012**, *5*, 7050.

(3) Moura de Salles Pupo, M.; Kortlever, R. Electrolyte Effects on the Electrochemical Reduction of CO_2. *ChemPhysChem* **2019**, *20*, 2926−2935.

(4) Vennekötter, J.-B.; Scheuermann, T.; Sengpiel, R.; Wessling, M. The electrolyte matters: Stable systems for high rate electrochemical CO_2 reduction. *J. CO2 Util.* **2019**, *32*, 202−213.

(5) Marcandalli, G.; Monteiro, M. C. O.; Goyal, A.; Koper, M. T. M. Electrolyte Effects on CO_2 Electrochemical Reduction to CO. *Acc. Chem. Res.* **2022**, *55*, 1900−1911.

(6) Xu, A.; Govindarajan, N.; Kastlunger, G.; Vijay, S.; Chan, K. Theories for Electrolyte Effects in CO_2 Electroreduction. *Acc. Chem. Res.* **2022**, *55*, 495−503.

(7) Deng, B.; Huang, M.; Zhao, X.; Mou, S.; Dong, F. Interfacial Electrolyte Effects on Electrocatalytic CO_2 Reduction. *ACS Catal.* **2022**, *12*, 331−362.

(8) Hori, Y.; Takahashi, R.; Yoshinami, Y.; Murata, A. Electrochemical Reduction of CO at a Copper Electrode. *J. Phys. Chem. B* **1997**, *101*, 7075−7081.

(9) Nitopi, S.; Bertheussen, E.; Scott, S. B.; Liu, X.; Engstfeld, A. K.; Horch, S.; Seger, B.; Stephens, I. E. L.; Chan, K.; Hahn, C.; et al. Progress and Perspectives of Electrochemical CO_2 Reduction on Copper in Aqueous Electrolyte. *Chem. Rev.* **2019**, *119*, 7610−7672.

(10) Huang, J. E.; Li, F.; Ozden, A.; Sedighian Rasouli, A.; García de Arquer, F. P.; Liu, S.; Zhang, S.; Luo, M.; Wang, X.; Lum, Y.; et al. CO_2 electrolysis to multicarbon products in strong acid. *Science* **2021**, *372*, 1074−1078.

(11) Zhu, X.; Huang, J.; Eikerling, M. Electrochemical CO_2 Reduction at Silver from a Local Perspective. *ACS Catal.* **2021**, *11*, 14521−14532.

(12) Dunwell, M.; Lu, Q.; Heyes, J. M.; Rosen, J.; Chen, J. G.; Yan, Y.; Jiao, F.; Xu, B. The Central Role of Bicarbonate in the Electrochemical Reduction of Carbon Dioxide on Gold. *J. Am. Chem. Soc.* **2017**, *139*, 3774−3783.

(13) Waegele, M. M.; Gunathunge, C. M.; Li, J.; Li, X. How cations affect the electric double layer and the rates and selectivity of electrocatalytic processes. *J. Chem. Phys.* **2019**, *151*, No. 160902.

(14) Zhang, F.; Co, A. C. Direct Evidence of Local pH Change and the Role of Alkali Cation during CO_2 Electroreduction in Aqueous Media. *Angew. Chem., Int. Ed.* **2020**, *59*, 1674−1681, DOI: 10.1002/anie.201912637.

(15) Murata, A.; Hori, Y. Product Selectivity Affected by Cationic Species in Electrochemical Reduction of CO_2 and CO at a Cu Electrode. *Bull. Chem. Soc. Jpn.* **1991**, *64*, 123−127.

(16) Singh, M. R.; Kwon, Y.; Lum, Y.; Ager, J. W.; Bell, A. T. Hydrolysis of Electrolyte Cations Enhances the Electrochemical Reduction of CO_2 over Ag and Cu. *J. Am. Chem. Soc.* **2016**, *138*, 13006−13012.

(17) Resasco, J.; Chen, L. D.; Clark, E.; Tsai, C.; Hahn, C.; Jaramillo, T. F.; Chan, K.; Bell, A. T. Promoter Effects of Alkali Metal Cations on the Electrochemical Reduction of Carbon Dioxide. *J. Am. Chem. Soc.* **2017**, *139*, 11277−11287.

(18) Monteiro, M. C.; Koper, M. T. Measuring local pH in electrochemistry. *Curr. Opin. Electrochem.* **2021**, *25*, No. 100649.

(19) Ayemoba, O.; Cuesta, A. Spectroscopic Evidence of Size-Dependent Buffering of Interfacial pH by Cation Hydrolysis during CO_2 Electroreduction. *ACS Appl. Mater. Interfaces* **2017**, *9*, 27377−27382.

(20) Malkani, A. S.; Anibal, J.; Xu, B. Cation Effect on Interfacial CO_2 Concentration in the Electrochemical CO_2 Reduction Reaction. *ACS Catal.* **2020**, *10*, 14871−14876.
(21) Dieckhöfer, S.; Öhl, D.; Junqueira, J. R.; Quast, T.; Turek, T.; Schuhmann, W. Probing the Local Reaction Environment During High Turnover Carbon Dioxide Reduction with Ag-Based Gas Diffusion Electrodes. *Chem. - Eur. J.* **2021**, *27*, 5906−5912, DOI: 10.1002/chem.202100387.
(22) Monteiro, M. C. O.; Mirabal, A.; Jacobse, L.; Doblhoff-Dier, K.; Barton, S. C.; Koper, M. T. M. Time-Resolved Local pH Measurements during CO_2 Reduction Using Scanning Electrochemical Microscopy: Buffering and Tip Effects. *JACS Au* **2021**, *1*, 1915−1924.
(23) Yang, K.; Kas, R.; Smith, W. A. *In Situ* Infrared Spectroscopy Reveals Persistent Alkalinity near Electrode Surfaces during CO_2 Electroreduction. *J. Am. Chem. Soc.* **2019**, *141*, 15891−15900.
(24) Henckel, D. A.; Counihan, M. J.; Holmes, H. E.; Chen, X.; Nwabara, U. O.; Verma, S.; Rodríguez-López, J.; Kenis, P. J. A.; Gewirth, A. A. Potential Dependence of the Local pH in a CO_2 Reduction Electrolyzer. *ACS Catal.* **2021**, *11*, 255−263.
(25) Welch, A. J.; Fenwick, A. Q.; Böhme, A.; Chen, H.-Y.; Sullivan, I.; Li, X.; DuChene, J. S.; Xiang, C.; Atwater, H. A. *Operando* Local pH Measurement within Gas Diffusion Electrodes Performing Electrochemical Carbon Dioxide Reduction. *J. Phys. Chem. C* **2021**, *125*, 20896−20904.
(26) Lu, X.; Zhu, C.; Wu, Z.; Xuan, J.; Francisco, J. S.; Wang, H. *In Situ* Observation of the pH Gradient near the Gas Diffusion Electrode of CO_2 Reduction in Alkaline Electrolyte. *J. Am. Chem. Soc.* **2020**, *142*, 15438−15444.
(27) Schatz, M.; Jovanovic, S.; Eichel, R.-A.; Granwehr, J. Quantifying local pH changes in carbonate electrolyte during copper-catalysed CO_2 electroreduction using *in operando* ^{13}C NMR. *Sci. Rep.* **2022**, *12*, No. 8274.
(28) Jovanovic, S.; Schleker, P. P.; Streun, M.; Merz, S.; Jakes, P.; Schatz, M.; Eichel, R.-A.; Granwehr, J. An electrochemical cell for *in operando* ^{13}C nuclear magnetic resonance investigations of carbon dioxide/carbonate processes in aqueous solution. *Magn. Reson.* **2021**, *2*, 265−280, DOI: 10.5194/mr-2-265-2021.
(29) Chandrashekar, S.; Trease, N. M.; Chang, H. J.; Du, L.-S.; Grey, C. P.; Jerschow, A. ^7Li MRI of Li batteries reveals location of microstructural lithium. *Nat. Mater.* **2012**, *11*, 311−315.
(30) Romanenko, K.; Forsyth, M.; O'Dell, L. A. New opportunities for quantitative and time efficient 3D MRI of liquid and solid electrochemical cell components: Sectoral Fast Spin Echo and SPRITE. *J. Magn. Reson.* **2014**, *248*, 96−104, DOI: 10.1016/j.jmr.2014.09.017.
(31) Hori, Y.; Konishi, H.; Futamura, T.; Murata, A.; Koga, O.; Sakurai, H.; Oguma, K. Deactivation of copper electrode" in electrochemical reduction of CO_2. *Electrochim. Acta* **2005**, *50*, 5354−5369.
(32) Li, D.; Li, N.; Xia, G.; Zheng, Z.; Wang, J.; Xiao, N.; Zhai, W.; Wu, G. An in-situ study of copper electropolishing in phosphoric acid solution. *Int. J. Electrochem. Sci.* **2013**, *8*, 1041−1046, DOI: 10.1016/S1452-3981(23)14078-8.
(33) Hori, Y.; Murata, A.; Takahashi, R. Formation of hydrocarbons in the electrochemical reduction of carbon dioxide at a copper electrode in aqueous solution. *J. Chem. Soc., Faraday Trans. 1* **1989**, *85*, 2309−2326, DOI: 10.1039/f19898502309.
(34) Jiang, G.; Han, D.; Han, Z.; Gao, J.; Wang, X.; Weng, Z.; Yang, Q.-H. Rational Manipulation of Intermediates on Copper for CO_2 Electroreduction Toward Multicarbon Products. *Trans. Tianjin Univ.* **2022**, *28*, 265−291, DOI: 10.1007/s12209-022-00330-1.
(35) Klamor, S.; Zick, K.; Oerther, T.; Schappacher, F. M.; Winter, M.; Brunklaus, G. ^7Li *in situ* 1D NMR imaging of a lithium ion battery. *Phys. Chem. Chem. Phys.* **2015**, *17*, 4458−4465.
(36) Britton, M. M. Magnetic resonance imaging of electrochemical cells containing bulk metal. *ChemPhysChem* **2014**, *15*, 1731−1736.
(37) Edwards, T. J.; Maurer, G.; Newman, J.; Prausnitz, J. M. Vapor-liquid equilibria in multicomponent aqueous solutions of volatile weak electrolytes. *AIChE J.* **1978**, *24*, 966−976.
(38) Adams, R. W.; Holroyd, C. M.; Aguilar, J. A.; Nilsson, M.; Morris, G. A. Perfecting WATERGATE: clean proton NMR spectra from aqueous solution. *Chem. Commun.* **2013**, *49*, 358−360.
(39) Benders, S.; Gomes, B. F.; Carmo, M.; Colnago, L. A.; Blümich, B. In-situ MRI velocimetry of the magnetohydrodynamic effect in electrochemical cells. *J. Magn. Reson.* **2020**, *312*, 106692 DOI: 10.1016/j.jmr.2020.106692.
(40) Matsushima, H.; Iida, T.; Fukunaka, Y. Gas bubble evolution on transparent electrode during water electrolysis in a magnetic field. *Electrochim. Acta* **2013**, *100*, 261−264.
(41) Deverell, C.; Richards, R. E. Nuclear magnetic resonance studies of alkali metal halide solutions. *Mol. Phys.* **1966**, *10*, 551−564.
(42) Luo, Z.-X.; Xing, Y.-Z.; Liu, S.; Ling, Y.-C.; Kleinhammes, A.; Wu, Y. Dehydration of Ions in Voltage-Gated Carbon Nanopores Observed by in Situ NMR. *J. Phys. Chem. Lett.* **2015**, *6*, 5022−5026.
(43) Heenen, H. H.; Shin, H.; Kastlunger, G.; Overa, S.; Gauthier, J. A.; Jiao, F.; Chan, K. The mechanism for acetate formation in electrochemical CO_2 reduction on Cu: selectivity with potential, pH, and nanostructuring. *Energy Environ. Sci.* **2022**, *15*, 3978−3990.